Astronomy
&
Astrophysics

Herschel-Planck dust optical depth and column density maps

II. Perseus⋆

Eleonora Zari[1,2], Marco Lombardi[2], João Alves[3], Charles J. Lada[4], and Hervé Bouy[5]

[1] Leiden Observatory, Niels Bohrweg 2, 2333 CA Leiden, The Netherlands
   e-mail: zariem@strw.leidenuniv.nl
[2] University of Milan, Department of Physics, via Celoria 16, 20133 Milan, Italy
[3] University of Vienna, Turkenschanzstrasse 17, 1180 Vienna, Austria
[4] Harvard-Smithsonian Center for Astrophysics, Mail Stop 72, 60 Garden Street, Cambridge, MA 02138, USA
[5] Centro de Astrobiología, INTA-CSIC, PO Box 78, 28691 Villanueva de la Canada, Madrid, Spain

Received 25 May 2015 / Accepted 24 November 2015

ABSTRACT

We present optical depth and temperature maps of the Perseus molecular cloud, obtained combining dust emission data from the *Herschel* and *Planck* satellites and 2MASS/NIR dust extinction maps. The maps have a resolution of 36 arcsec in the *Herschel* regions, and of 5 arcmin elsewhere. The dynamic range of the optical depth map ranges from 1×10^{-2} mag up to 20 mag in the equivalent K-band extinction. We also evaluate the ratio between the 2.2 μm extinction coefficient and the 850 μm opacity. The value we obtain is close to the one found in the Orion B molecular cloud. We show that the cumulative and the differential area function of the data (which is proportional to the probability distribution function of the cloud column density) follow power laws with an index of respectively $\simeq -2$, and $\simeq -3$. We use WISE data to improve current YSO catalogs based mostly on *Spitzer* data and we build an up-to-date selection of Class I/0 objects. Using this selection, we evaluate the local Schmidt law, $\Sigma_{YSO} \propto \Sigma_{gas}^{\beta}$, showing that $\beta = 2.4 \pm 0.6$. Finally, we show that the area-extinction relation is important for determining the star-formation rate in the cloud, which is in agreement with other recent works.

Key words. ISM: clouds – dust, extinction – ISM: individual objects: Perseus molecular could – methods: data analysis – ISM: structure

1. Introduction

Understanding the physical processes that govern star formation is fundamental to improving our knowledge of galaxy formation and evolution across cosmic time. An essential step towards reaching a better comprehension of star formation inside our Galaxy is to establish the relationship between the star-formation rate (SFR) and the physical properties of the interstellar gas. Schmidt (1959) conjectured that "the SFR depends on the gas density and [...] varies with a power law of the gas density". Schmidt argued that the index of the power law in the solar neighbourhood was ∼2. Kennicutt (1998) expressed the law as $\Sigma_{SFR} = \kappa \Sigma_{gas}^{\beta}$, where Σ_{gas} and Σ_{SFR} are the surface densities of the gas and of star-formation rate. Kennicutt tested the Schmidt law in a heterogeneous sample of star-forming galaxies and showed that a power-law scaling relation exists between them and is characterised by an index β = 1.6. Using observations of local disc and starburst galaxies, Bigiel et al. (2008) found a complex scaling between Σ_{SFR} and Σ_{gas}, which could not be described by a single power law. On smaller, sub-kpc scales, Lada et al. (2013) showed that there is no Schmidt scaling relation between local giant molecular clouds, but a series of observational studies demonstrated that a Schmidt scaling law exists within some local molecular clouds (Heiderman et al. 2010; Gutermuth et al. 2011; Lombardi et al. 2013; Lada et al. 2013; Evans et al. 2014; Harvey et al. 2014).

To be able to understand the detailed interplay between the structure of molecular clouds and their local star formation rates (as opposed to the global one that is often considered), we carry out a coordinated study of molecular clouds in the Gould belt. We use a combination of *Planck* and *Herschel* dust emission data, calibrated using near-infrared (NIR) dust extinction. This technique guarantees an optimal resolution of the cloud column density maps (which corresponds with the *Herschel*/SPIRE 500 36 arcsec resolution), better than that of standard NIR extinction maps in the region of the sky we consider. In our first paper we considered the Orion giant molecular cloud (Lombardi et al. 2014); here we focus on Perseus.

The Perseus cloud was first observed by Barnard, who catalogued a portion of it as Barnard 1-5 and Barnard 202-206. Since then, the cloud has been extensively studied using molecular line emission (Ridge et al. 2006), star count extinction (Bachiller & Cernicharo 1984), and dust continuum emission (Hatchell et al. 2005; Kirk et al. 2006; Enoch et al. 2006). Distance estimates for Perseus vary (Herbig & Jones 1983; Cernis 1990, 1993; Bally et al. 2008; Hirota et al. 2008; Schlafly et al. 2014); we use 240 pc for consistency with Lombardi et al. (2010). Perseus is the prototype intermediate

---

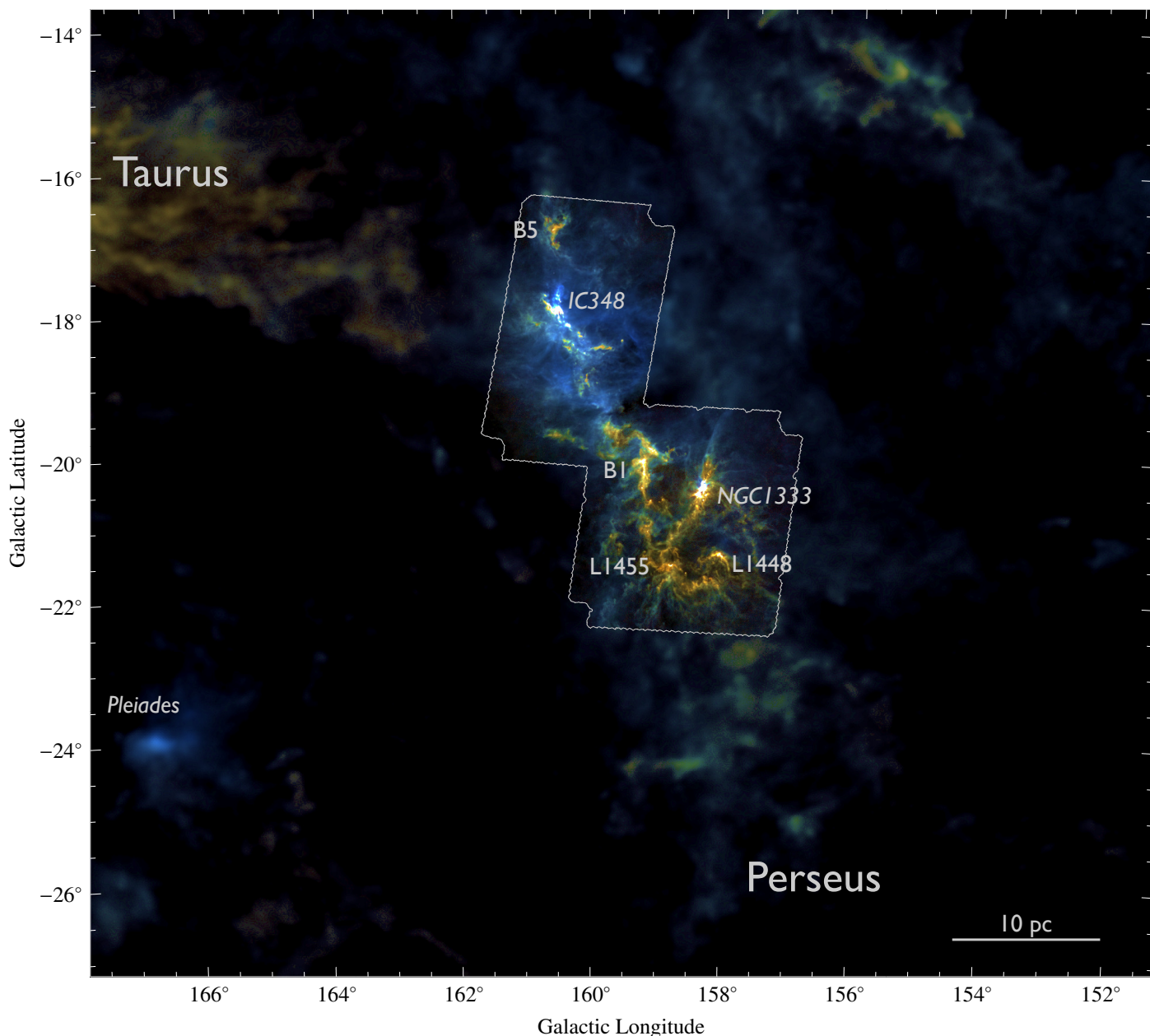⋆ The optical depth and temperature maps (FITS files) are only available at the CDS via anonymous ftp to cdsarc.u-strasbg.fr (130.79.128.5) or via http://cdsarc.u-strasbg.fr/viz-bin/qcat?J/A+A/587/A106

Fig. 1. Composite three-colour image showing *Herschel*/SPIRE intensities for the region considered, where available (with the 250 μm; 350 μm; 500 μm bands shown in blue, green, and red). For regions outside the *Herschel* coverage, we used the *Planck*/IRAS dust model (τ_{850}, T, β) to predict the intensity that would be observed at the SPIRE passbands. Toggle labels

mass star-forming region, with young B stars and two clusters, IC 348 (Muench et al. 2007) and NGC 1333 (Lada et al. 1996). The complex seems to be associated with the Perseus OB2 association (de Zeeuw et al. 1999). Recently, *Herschel* observations were used to characterise small regions of the cloud. Pezzuto et al. (2012) studied two star-forming dust condensations, B1-bS and B1-bN, in the B1 region (see Fig. 1). They conclude that these two sources could be good examples of the first hydrostatic core phase. Sadavoy et al. (2012) present observations of the B1-E region and propose that it may be forming the first generation of dense cores. Finally, Sadavoy et al. (2014) identified and characterised 28 candidate Class 0 protostars in the whole cloud, four of which are newly discovered. They also found that the star-formation efficiency of the clumps, as traced by Class 0 protostars, correlates strongly with the flatness of their respective column density distribution at high values. A global

study of the Perseus cloud properties with *Herschel* data is still missing, and constitutes the main goal of this paper.

This paper is organised as follows. In Sect. 2 we present the data used in this work; in Sect. 3 we briefly describe the data-reduction process; in Sect. 4 we apply the method to study the Perseus molecular cloud and present the column density and temperature maps[1]; in Sect. 5 we derive the local Schmidt law; finally, in Sect. 6 we present a summary.

2. Data

Perseus was observed as part of the Gould Belt Survey (André et al. 2010), one of the *Herschel* satellite key projects.

---

[1] The maps will be publicly available through CDS (http://cdsweb.u-strasbg.fr) and the website http://www.interstellarclouds.org

Table 1. *Herschel* parallel mode observation used.

Target name	Obs. ID	RA	Dec	Wavelengths (μm)	Obs. date	Exp. time (s)
Perseus S	1342190326	3h 29m 38s	+30 54′ 33″	SPIRE, PACS 70 and 160	2010-09-02	14 765
Perseus N	1342214504	3h 42m 51s	+32 01′ 38″	SPIRE, PACS 70 and 160	2011-19-2	11 624

The cloud was observed using the two photometers PACS (Poglitsch et al. 2010) and SPIRE (Griffin et al. 2010), in five bands, centered approximately at 70 μm; 160 μm; 250 μm; 350 μm; 500 μm. Table 1 gives an overview of the observation used in this work. Dust maps derived by the *Planck* Collaboration (Planck Collaboration XI 2014), and the NIR extinction maps that were produced by Lombardi et al. (2010) through the NICEST method (Lombardi 2009) are also used. We selected the region (corresponding to the Perseus molecular cloud) with galactic coordinates

$$155° < l < 165°, \qquad -25° < b < -15°. \tag{1}$$

Additionally, we employed the AllWISE data release (Wright et al. 2010; Mainzer et al. 2011) to select young stellar objects (YSOs) from their colours. The WISE satellite observed the whole sky in four infrared bands, often referred to as $W1$, $W2$, $W3$, and $W4$, with wavelengths centred at 3.4 μm; 4.6 μm; 12 μm; 22 μm. We retrieved 1.43 million sources from the WISE point source catalog in the science field and 1.63 million sources in the control field. We rejected any source with contamination and confusion flags and we further restricted the selection to those measurements with errors $\sigma < 0.15$ mag in all the WISE bands. The AllWISE source catalog contains associations with the 2MASS Point Source Catalog (Skrutskie et al. 2006). The precision adopted by the AllWISE collaboration for the 2MASS association is 3″. In addition, we required photometric errors in the 2MASS bands to be less than 0.1 mag.

3. Method

The reduction technique is very close to the one presented by Lombardi et al. (2014) and therefore we only briefly summarise it in this section.

3.1. Dust model

Dust is optically thin at the *Herschel* observation frequencies (at least for $\lambda > 160$ μm), and therefore its emission can be modelled as a modified black body:

$$I_\nu = B_\nu(T)(1 - e^{-\tau_\nu}) \simeq B_\nu(T)\,\tau_\nu. \tag{2}$$

Here $B_\nu(T)$ is the black-body function at the temperature T and the optical thickness τ_ν is taken to be a power law of the frequency ν:

$$\tau_\nu = \tau_{\nu_0}\left(\frac{\nu}{\nu_0}\right)^\beta. \tag{3}$$

The frequency ν_0 is an arbitrary reference frequency that we set as $\nu_0 = 353$ GHz (corresponding to $\lambda = 850$ μm), which is similar to what was done by the *Planck* collaboration (Planck Collaboration XI 2014).

3.2. Spectral energy distribution fitting

The aim of our work is to infer the effective dust colour temperature and the optical depth from the fluxes measured by *Herschel* at 250 μm; 350 μm; 500 μm, following Lombardi et al. (2014), and also PACS 160 μm where available. For this purpose, we first convolved all the *Herschel* data to the beam size of SPIRE 500 μm, i.e. to 36 arcsec and then we fitted the observed spectral energy distribution (SED) with the function (2), that was integrated over the *Herschel* bandpasses. The fitting procedure is described in detail in Lombardi et al. (2014). We report here, however, a brief outline of the basic steps used to generate the maps:

– For each SPIRE band we multiply by the correcting factor $C = K_{4e}/K_{4p}$. Since the extended source calibration method changed as a consequence of the work by Griffin et al. (2013), the correcting factors are not the same as those used in Lombardi et al. (2014). Specifically, C is now equal to (0.9986, 1.0015, 0.9993), while before it was $C = (0.9828, 0.9834, 0.9710)$ for the 250 μm; 350 μm; 500 μm bands respectively. However, this change doesn't have a significant impact on the final maps.
– We perform an absolute flux calibration for the *Herschel* bands, using *Planck* maps.
– We assume a modified black-body SED and we compute the expected flux at each reference passband.
– We modify the SED until we obtain a good match between the observed and theoretical fluxes. For this step we use a simple χ^2 minimization technique that takes into account the calibration errors.

For the analysis presented here, we used the HIPE (Ott 2010) extended emission level 2.5 products for SPIRE data and Unimaps for PACS data. For PACS data, it is possible to use Scanamorphos. However there is no significant difference between the two maps.

Figure 1 shows a colour-composite image of the combined reduced *Herschel*/SPIRE data for the region we considered, together with the predicted fluxes from *Planck* at the three SPIRE passbands for locations outside the *Herschel* coverage.

3.3. Optical depth and temperature maps

Figure 2 shows the combined optical depth-temperature map: the effective dust temperature is represented using different values of hue, while the intensity is proportional to the optical depth. Figures 3 and 4 individually show the temperature and optical depth maps.

Note that *Planck* data have lower resolution (5 arcmin instead of 36 arcsec) and a significantly lower noise. In particular, the error in the regions covered by *Planck* data is much smaller than that on the *Herschel* areas. Figures 3 and 4 highlight the differences in optical depth and temperature that characterise the cloud.

Referring to the temperature map (Fig. 4), we note that the regions IC 348 and G159.6-18.5 present a higher temperature than the rest of the cloud, and that the ring of dust that surrounds
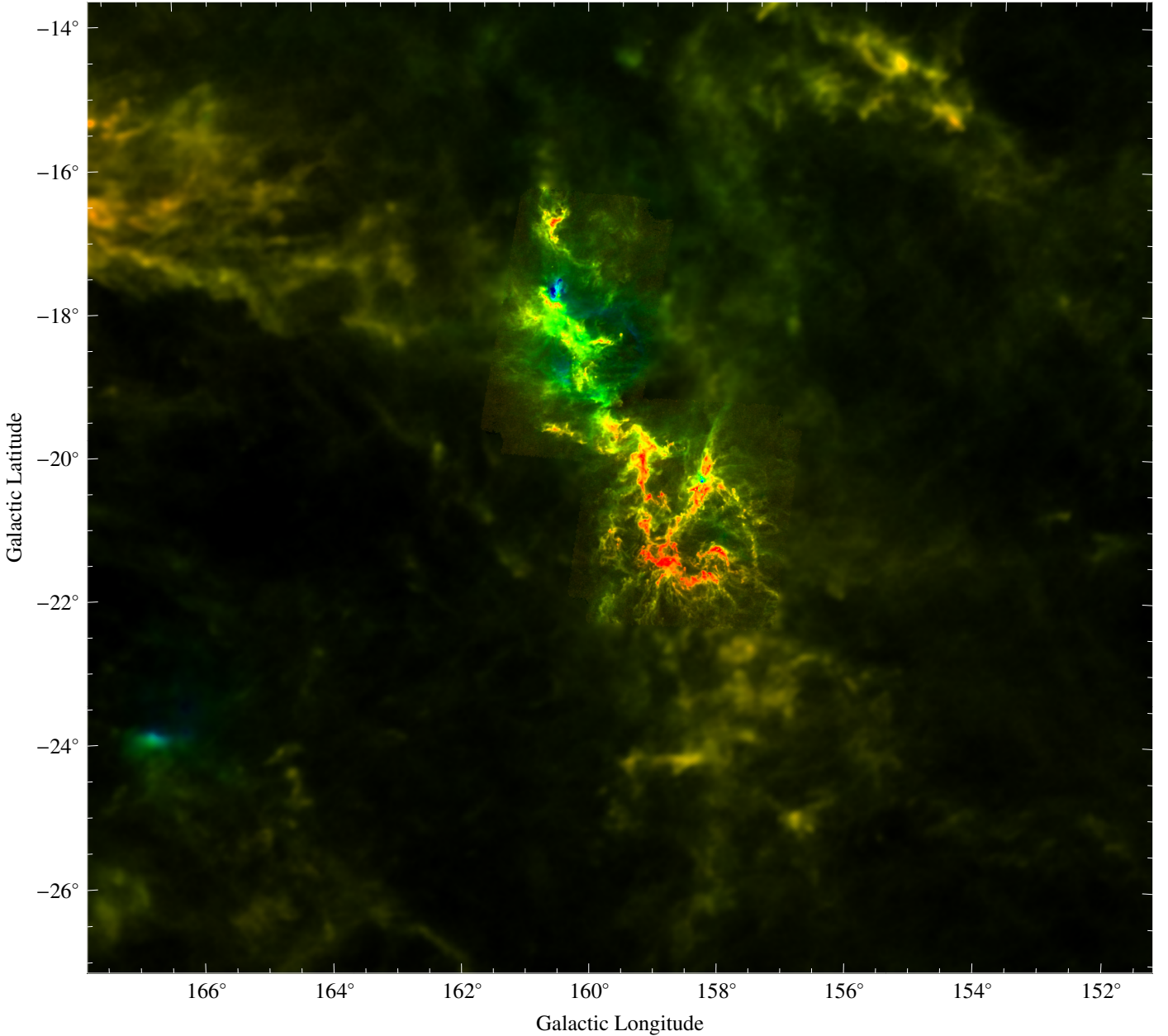
Fig. 2. Combined optical depth-temperature map for Perseus. The image shows the optical depth as intensity and the temperature as hue, with red (blue) corresponding to low (high) temperatures.

the star HD 278942 (Andersson et al. 2000) is particularly visible. The temperature ranges between ~10 K and ~36 K.

3.4. Extinction conversion

To compare the results obtained here with other observations, we converted the optical depth τ_{850} to the extinction A_K. For this purpose, we smoothed the optical depth map to the same resolution as the extinction map (2.5 arcmin) of the region (Lombardi et al. 2010). We assumed that within the range $0-2 \times 10^{-4}$, the law that describes the relation between τ_{850} and A_K is linear (see Fig. 5):

$$A_K = \gamma \tau_{850} + \delta. \tag{4}$$

The slope γ is proportional to the opacity κ_{850} and to the extinction coefficient in the K-band, $C_{2.2}$. Since the extinction in the

K-band is defined as

$$A_K = -2.5 \log_{10}\left(\frac{I_{\mathrm{obs}}}{I_{\mathrm{true}}}\right) = 2.5(\log_{10} e) C_{2.2}\Sigma_{\mathrm{dust}}, \tag{5}$$

the relationship between γ and $C_{2.2}$ is simply $\gamma \simeq 1.0857\, C_{2.2}/\kappa_{850}$. The coefficient δ is associated with uncertainties in the absolute flux calibration of Herschel, or to uncertainties in the extinction maps, or both. Through a χ^2 minimization method, we obtained the following values for the two parameters:

$$\begin{cases} \gamma = 3931 \pm 274\,\mathrm{mag}, \\ \delta = -0.05 \pm -0.02 \times 10^{-6}\,\mathrm{mag}. \end{cases} \tag{6}$$

The fact that δ is close to zero confirms the goodness of the calibration of *Herschel* data and of the extinction map. The value obtained for the slope γ is quite close to those found by
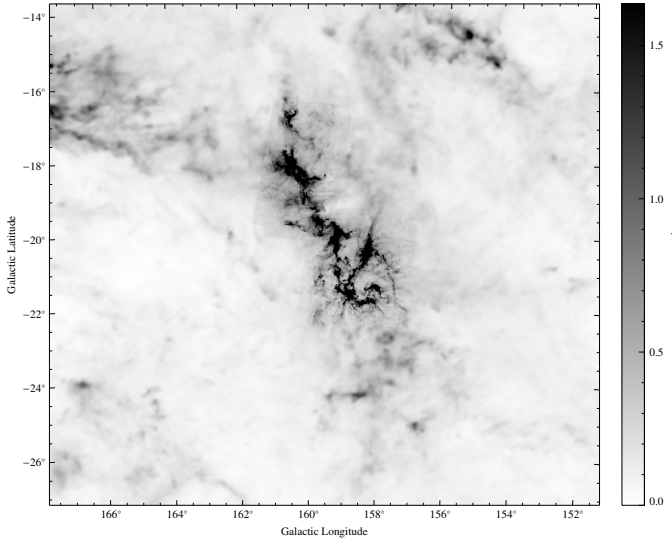
Fig. 3. Optical depth map of the field and, on a ¦different layer¦, the corresponding error map. This figure, as for the following one (Fig. 3), is produced by the method described in the text, using the reduced fluxes of SPIRE and the expected fluxes at SPIRE frequencies that were deduced from the *Planck* maps (Planck Collaboration XI 2014).
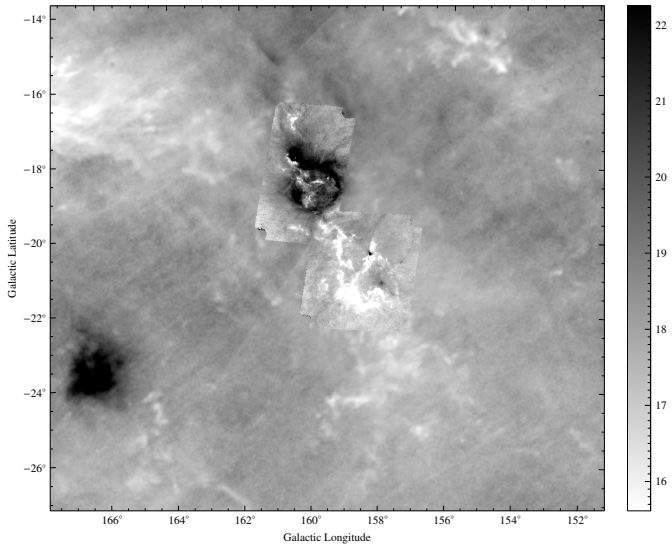

Fig. 4. Temperature map of the field and, on a ¦different layer¦, the corresponding error map.

Lombardi et al. (2014) for Orion A and B ($\gamma_{\rm Orion\,A} = 2640$ mag and $\gamma_{\rm Orion\,B} = 3460$ mag). Being proportional to the extinction coefficient $C_{2.2}$ and the opacity at 850 μm, the coefficient γ is related to the dust composition and grain distribution, and therefore differences in the values of γ are likely related to differences in these quantities.

If we consider a wider range of values (see Fig. A.3), with $\tau \times 10^4 \leq 10$, the relation unexpectedly deviates from the linear law. In this case, the law between τ_{850} and A_K can be fitted by the empirical relation:

$$A_K = c_1 + c_2 \tau_{850}^{c_3}. \tag{7}$$

The best fit values for the three parameters are

$$\begin{cases} c_1 = -0.38447 \pm 6.9 \times 10^{-05} \text{ mag,} \\ c_2 = 61 \pm 5 \text{ mag,} \\ c_3 = 0.47973 \pm 2.6 \times 10^{-05}. \end{cases} \tag{8}$$
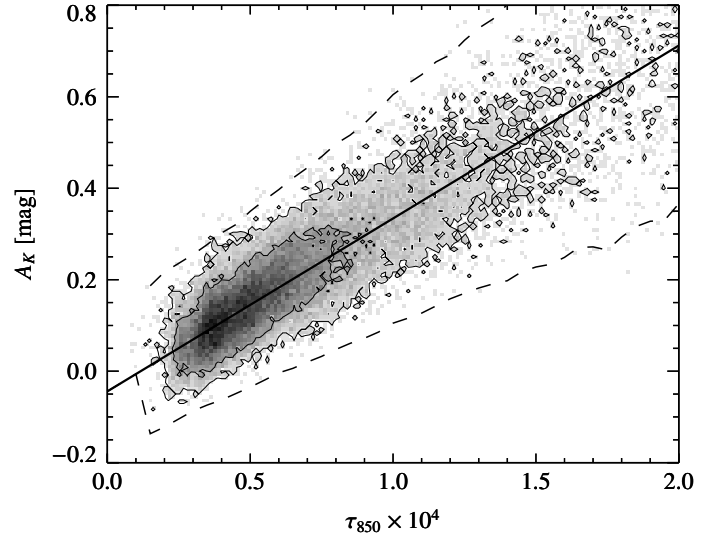

Fig. 5. Relationship between submillimitre optical depth and NIR extinction in Perseus. The image shows the best linear fit, used to calibrate the data (solid line), together with the expected 3σ region (dashed lines), as calculated from direct error propagation in the extinction map. The contours enclose the 68% and the 95% of the points, respectively.

The deviation from the linear regime might be due to either the inclusion of regions in the extinction map where a large number of embedded sources are present or the lack of background stars at highest extinction. To better understand the problem, we created a map (Fig. 6) that shows the difference between the extinction values evaluated from the extinction map and from the *Herschel* data using the linear scaling of Eq. (4). The highest discrepancies roughly coincide with the position of the Class 0 sources reported by Sadavoy et al. (2014). Since in these regions the difference is positive, it seems that the extinction map produced through 2MASS data with the NICEST method underestimates the extinction values in the densest regions, where the number of background stars is low and contamination from embedded sources may be present. For this reason we only consider the linear case Eq. (4) to convert optical depth values to extinction for our *Herschel* optical depths.

4. Results

To characterise the maps, we produced the integral area function of the cloud, $S(>A_K)$, i.e. the surface of the cloud above a certain extinction threshold as a function of that threshold. Lada et al. (2013) observed that the shape of the function $S(>A_K)$ and of its derivative, $S'(>A_K)$, influences the variation in the rate of star formation of the cloud, especially in the high-extinction regions.

The plot of $S(>A_K)$ is shown in Fig. 7 for different extinction measurements (*Herschel*, *Herschel* and *Planck*, 2MASS/ NICEST). In the same figure, a red line with slope -2 is represented. Operationally, this plot is built by just counting the sky area above different values of A_K. As such, the specific spacing used for the threshold A_K values is irrelevant (in Fig. 7 we used a log-scale in A_K). The law $S(>A_K) \propto A_K^{-2}$ appears to be an excellent description of the area function over two order of magnitudes, from $A_K \sim 0.1$ to $A_K \sim 10$ mag. The apparent break in this law at $A_K \sim 15$ mag might either be genuine or due to systematic effects in the *Herschel* maps (e.g. unresolved structures, large temperature gradients, flux contamination from point sources). At the other extreme, the break at $A_K < 0.15$ mag can be due
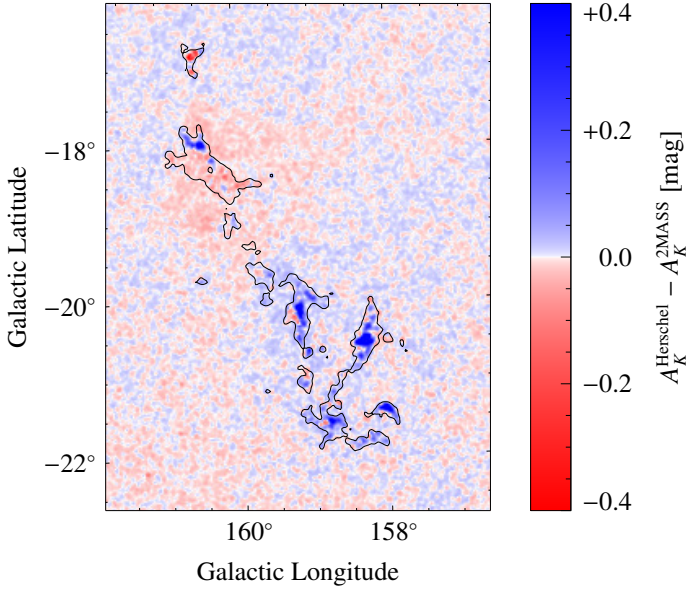
Fig. 6. Difference between the extinction values evaluated with the 2MASS/ NICEST map and the *Herschel* opacity map. The contour represents the $A_K = 0.5$ mag level.
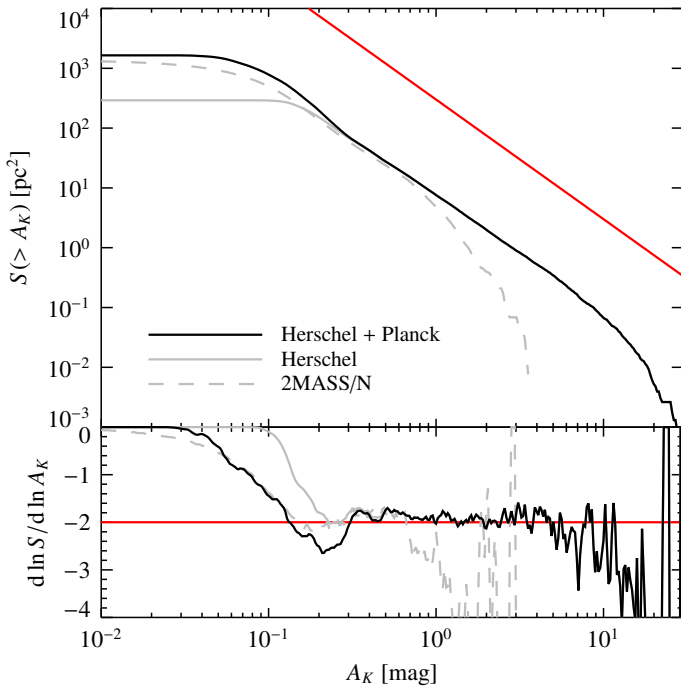

Fig. 7. Integral area-extinction relation for Perseus, i.e., the physical cloud area above a given extinction threshold as a function of that threshold. The solid black line shows the result for the entire field, while the solid gray line shows the same quantity for the *Herschel* regions. The dashed line shows again the same quantity, but for the 2MASS/NICEST data. The red line shows the slope of the power law $S(>A_K) \propto A_K^{-2}$.

to various effects, including contamination by unrelated foreground and background material, and inappropriate definition of the cloud boundaries. In reality, as shown by Lombardi et al. (2015), fundamental constraints, such as contamination by unrelated foreground and background dust emission, severely limit our ability to measure the area function below $A_K < 0.15$ mag.
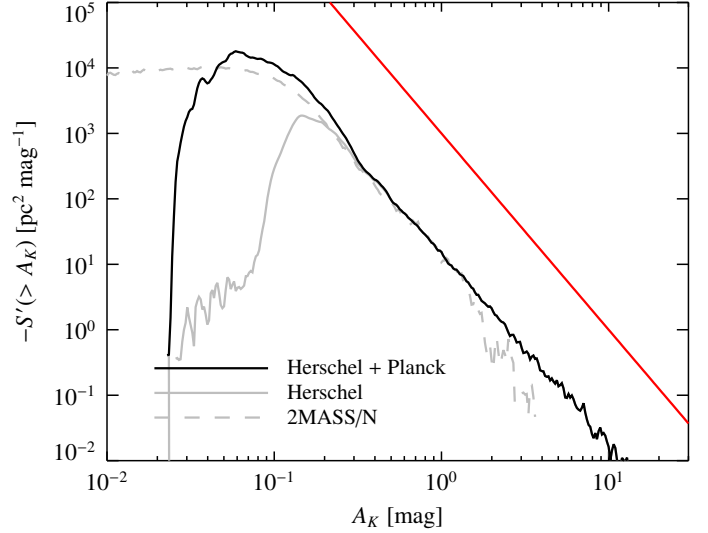
Fig. 8. Function $-S'(>A_K)$, i.e. the probability distribution function of the measured column density for Perseus. In this plot, a lognormal distribution would appear as a parabola and a power law as a straight line. The red line shows the slope of the power law $S'(>A_K) \propto A_K^{-3}$.
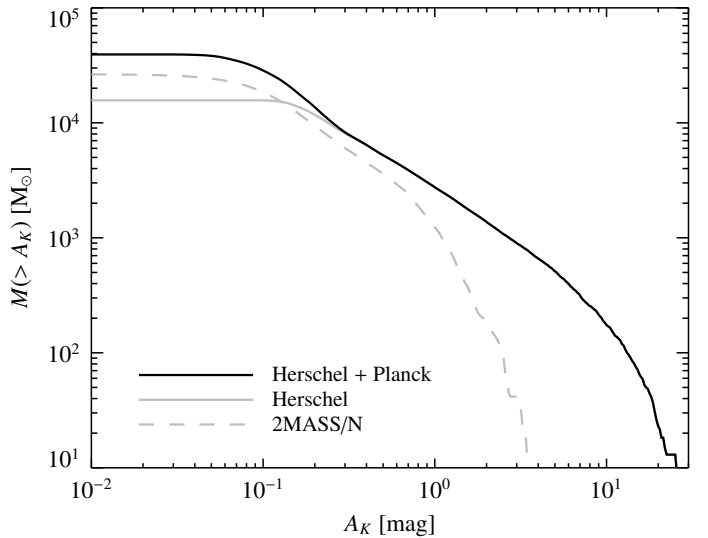

Fig. 9. Integral mass-extinction relation, i.e. the cloud mass above a given extinction threshold. The line codes follow the same convention as in Fig. 7. The values of the mass above a certain extinction threshold are listed in Table 2.

Figure 8 shows $-S'(>A_K)$ as a function of A_K, where A_K is evaluated through Eq. (4). This function is proportional to the probability distribution function (PDF) of the column density map and follows a power law with index equal to -3. Note that since we directly derived the function $S(>A_K)$ using a 3-point Lagrangian interpolation (where the spacing A_K is taken into account), this operation effectively produces a result that is proportional to a linearly-binned PDF. We stress that this differs from the choice adopted by Lombardi et al. (2015), where PDFs were logarithmically binned. Consequently, the slopes evaluated in this way differ by -1 to those presented by Lombardi et al. (2015), but the results are equivalent.

Figures 9 and 10 show the integral function of the mass $M(>A_K)$ as a function of A_K and its derivative $-M'(>A_K)$. The gas surface density, Σ_{gas}, can be expressed as a mass surface
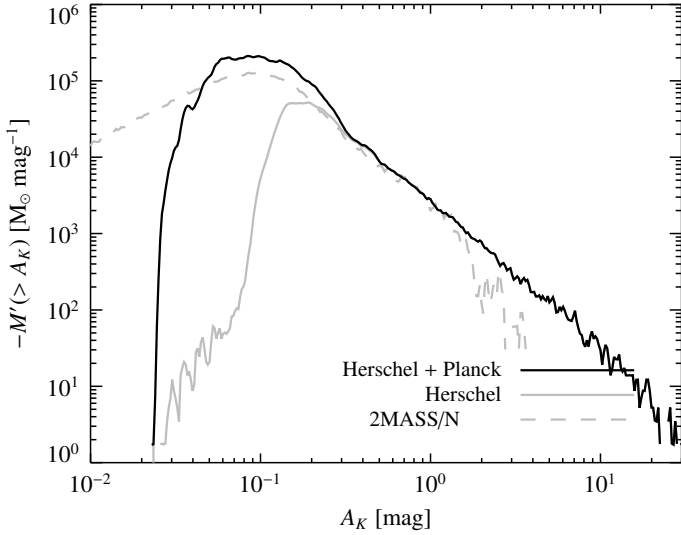
Fig. 10. Function $-M'(>A_K)$, i.e. the derivative of the integral mass function.

Table 2. Mass values above an extinction threshold, normalized at the mass at 0.1 mag, $M_{0.1}$.

A_K [mag]	M [$M_\odot$]	$M/M_{0.1}$
0.01	22 153	168%
0.1	13 189	100%
0.2	7864	60%
0.4	4956	37%
0.6	3685	27%
0.8	2887	21%
1.6	1532	11%
3.2	777	5%
6.4	341	2%

density through the following relation:

$$\frac{\Sigma_{\text{gas}}}{A_K} = \mu\, m_{\text{p}} \beta_K \simeq 183 \; M_\odot \,\text{pc}^{-2}\,\text{mag}^{-1}, \tag{9}$$

where $\mu = 1.37$ is the mean molecular weight, corrected for the helium abundance, $m_{\text{p}} = 1.67 \times 10^{-24}$ g is the proton mass and $\beta_K = 1.67 \times 10^{22}$ cm^{-2} mag^{-1} = $[2N\,(\text{H}_2) + N\,(\text{H}_I)]/A_K$ is the gas-to-dust ratio. The agreement between the solid line (*Herschel* and *Planck* data) and the dashed line (2MASS/ NICEST) in Figs. 7 and 9 is good until $A_K \simeq 0.1$ mag, while the discrepancy we observe at high extinction values is due to the higher levels of extinction reached by *Herschel*. Similar to Lombardi et al. (2014), we can define the mass of the cloud as the surface density integrated over the area

$$M = \int \Sigma_{\text{gas}}\, \text{d}S, \tag{10}$$

from which

$$M\,(>A_K) \propto \int_{A_K}^{\infty} \frac{\text{d}S\,(>A_K')}{\text{d}A_K'} A_K'\text{d}A_K'. \tag{11}$$

We note how the power-law trend observed in Fig. 9 is a direct consequence of the power law observed in Fig. 7, by replacing $\text{d}S\,(>A_K')/\text{d}A_K'$ with $A_K'^{-3}$ in Eq. (11).

5. The local Schmidt law

Another possible application of the column density maps is to study the validity of the Schmidt law (Schmidt 1959) in the Perseus molecular cloud. Half a century ago, Schmidt conjectured that the rate of star formation, Σ_{SFR}, depends on the (projected) gas density, Σ_{gas}, and in particular is a simple power law. Schmidt argued that the index of the power law was ~2. Recently, a series of observational studies (Lada 2015 and references therein) that use observations of protostellar objects, demonstrate that a Schmidt scaling law exists within a sample of nearby molecular clouds and it is typically characterised by an index ~2. In what follows we investigate the Schmidt law using, in particular, Class I and Class 0 protostars[2] to estimate the protostar surface density. Following Lada et al. (2013), we decided to consider only these types of sources, since they are still likely to be at, or close to, their original birth place. To estimate the protostar surface density, Σ_{YSO}, we used already existing catalogs based on *Spitzer* data and we built a catalog of YSOs through an analysis of the WISE satellite data. We used the WISE data mainly to enhance and improve the *Spitzer*-based catalogs. Indeed, even though WISE resolution (6.1″, 6.4″, 6.5″, and 12.0″ in the four bands) is lower than *Spitzer*, its all-sky coverage enables us to include sources detected in areas that were not surveyed by *Spitzer*. To make our classification as complete as possible, we also included the new sources detected by Sadavoy et al. (2014).

5.1. Identifying YSO candidates

The procedure adopted to search for YSO candidates is based on a comparison of the source distribution in several colour−colour diagrams between the science and a control field. We choose a control field in the region defined by

$$137° < l < 147° \qquad -25° < b < -15°. \tag{12}$$

We selected this area based on two requirements: it is characterised by low extinction values and the background object distribution is similar to that of the science field since it has the same galactic latitude of the science field, which corresponds to the region defined previously for 2MASS data. To classify the sources in the science field, we approximately followed the scheme proposed by Koenig et al. (2012), which in turn is based on the scheme by Gutermuth et al. (2008, 2009). Koenig analysed several WISE colour−colour diagrams of *Spitzer*-selected YSOs in the Taurus region. In addition, they characterised the contaminating sources by studying the distribution of objects with declination >88°.22 (celestial north pole) in the $W_1 - W_2$ vs. $W_2 - W_3$ colour−colour diagram. By comparing the science and the control field colour−colour diagrams, the presence in the science field of sources with colour excess can be noted: these may be reddened background objects or embedded YSOs. As Rebull et al. (2011) noted, no colour−colour diagram can perfectly find all the YSOs and remove all the contaminants: the contamination rate for any colour selection is expected to be large and ancillary data from other observations are often needed to choose the most likely candidates. Koenig et al. (2012) estimate a contamination rate for "typical" star-forming regions of about 2.4 objects resembling Class I YSOs, 3.8 objects resembling Class II YSOs, and 1.8 objects resembling transition discs per square degree. As a result, in our field, which is ~100 deg^2, the contaminants expected are respectively ~240, ~380, and ~180.

---

[2] In the following we will refer to Class I and 0 objects as *protostars*, and to Class II, Class I and Class 0 objects as *YSOs*.
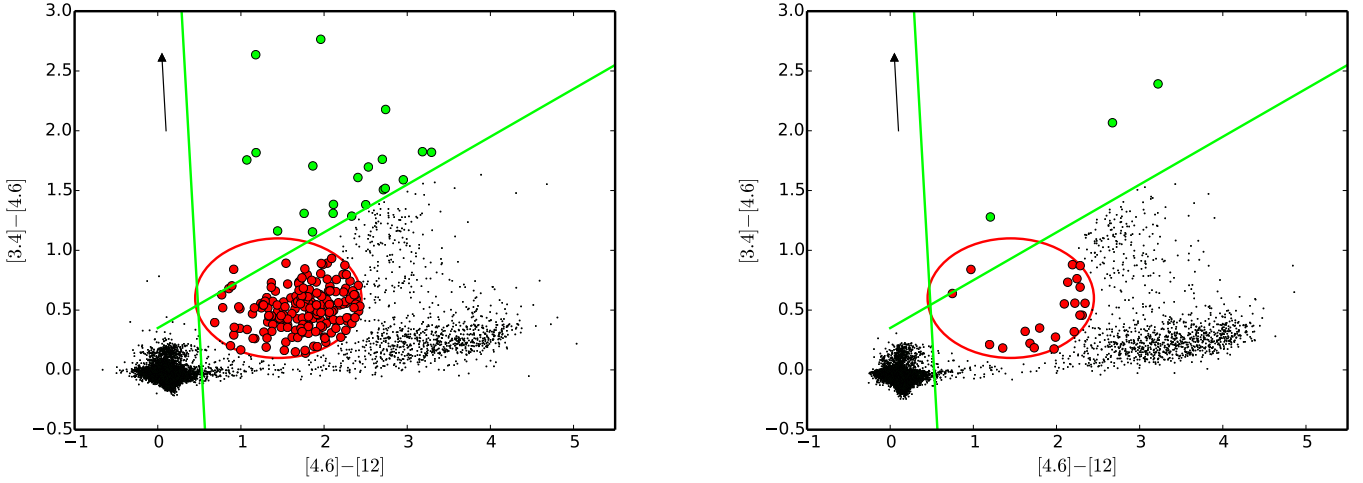
Fig. 11. $W1-W2$ ([3.4]−[4.6]) vs. $W2-W3$ ([4.6]−[12]) diagram for the science and the control field. Red points represent candidate Class II objects, green points represent candidate Class I objects, while black points represent the other sources in the field. The red ellipse and the green lines have equations specified in the text.
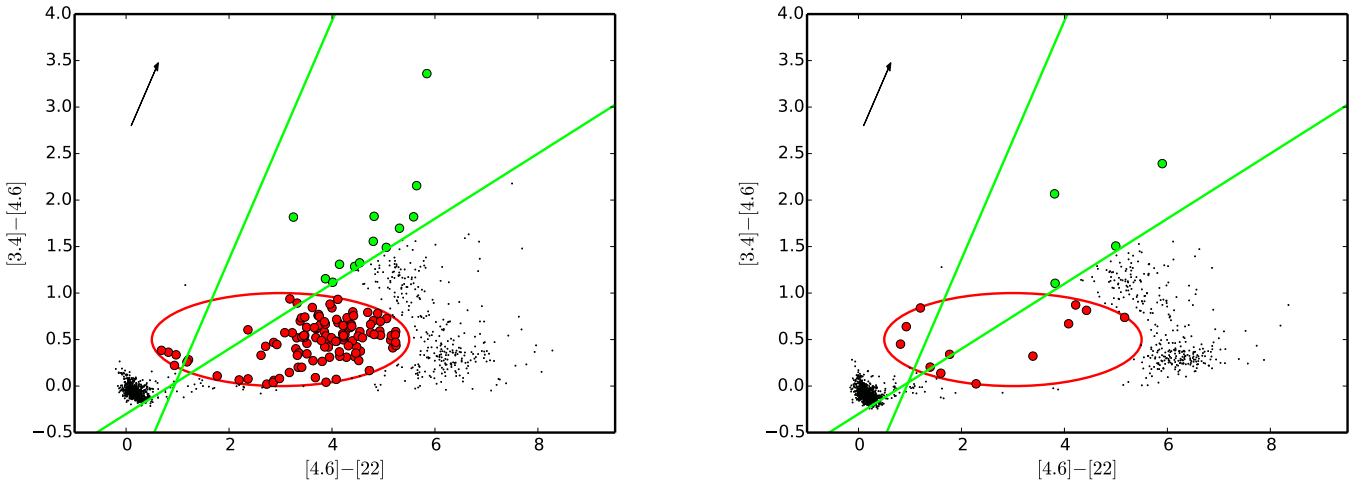

Fig. 12. $W1-W2$ vs. $W2-W4$ diagram of the science and the control field. Red points represent candidate Class II YSOs, green points represent candidate Class I protostars, while black points represent the other sources in the field. The red ellipse and the green slopes have equations specified in the text.

Figure 11 shows the colour−colour diagram in W_1, W_2, and W_3 bands of the science (left) and the control field (right). By comparing them, we observed a significant excess of sources inside the marked red ellipse with centre

$$\begin{cases} [4.6]-[12] = 1.45\,\text{mag}, \\ [3.4]-[4.6] = 0.6\,\text{mag} \end{cases} \tag{13}$$

and axes $a = 1$ mag and $b = 0.5$ mag, and between the two blue slopes with equations

$$\begin{cases} [3.4]-[4.6] = 0.4 \times ([4.6]-[12]) + 0.35\,\text{mag}, \\ [3.4]-[4.6] = -12.4 \times ([4.6]-[22]) + 6.3\,\text{mag}. \end{cases} \tag{14}$$

Therefore, we primarily select 213 objects inside these two regions. The reddening of the objects inside the ellipse is low, and we can therefore suppose that they are Class II YSOs. Instead, the objects lying between the two slopes (22) are highly reddened and can be classified as Class I protostars. We observe that the selected Class I protostars satisfy Koenig requirements. Furthermore, our classification is stricter since we remove all

sources in the AGN/galaxy region of the diagram, and the selection criteria of Class II YSOs are close to those chosen by Koenig et al. (2012). Indeed, the minimum colour values that were accepted to include a source in the selection are

$$\begin{cases} [4.6]-[12] = 0.95\,\text{mag}, \\ [3.4]-[4.6] = 0.35\,\text{mag}. \end{cases} \tag{15}$$

Figure 12 shows the diagrams [3.4]−[4.6] vs. [4.6]−[22] and is analogous to the previous one. Class II YSOs lie within the red ellipse, with centre

$$\begin{cases} [4.6]-[22] = 3\,\text{mag}, \\ [3.4]-[4.6] = 0.5\,\text{mag}, \end{cases} \tag{16}$$

and axes $a = 2.5$ mag and $b = 0.5$ mag, while Class I protostars are included between the slopes with equations

$$\begin{cases} [3.4]-[4.6] = 0.4 \times ([4.6]-[22]) - 0.3\,\text{mag}, \\ [3.4]-[4.6] = 1.3 \times ([4.6]-[22]) - 1.2\,\text{mag}. \end{cases} \tag{17}$$

The total number of sources is 130, with 117 of them classified as Class II YSOs, while the remaining 13 are classified as
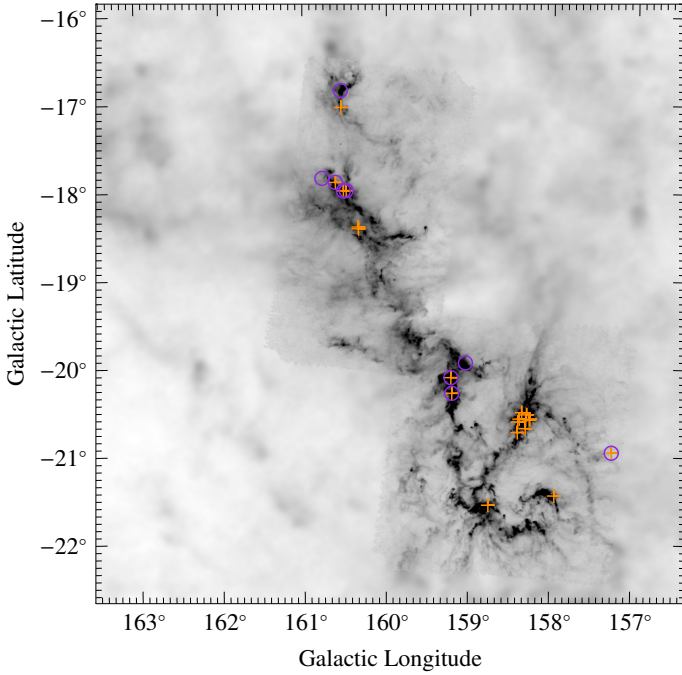
Fig. 13. Spatial distribution of candidate Class I objects (orange crosses) selected through the [3.4]−[4.6] vs. [4.6]−[12] colour−colour diagram and Class I objects (purple circles) selected through the [3.4]−[4.6] vs. [4.6]−[22] colour−colour diagram. The map shown here is the optical-depth map presented before.
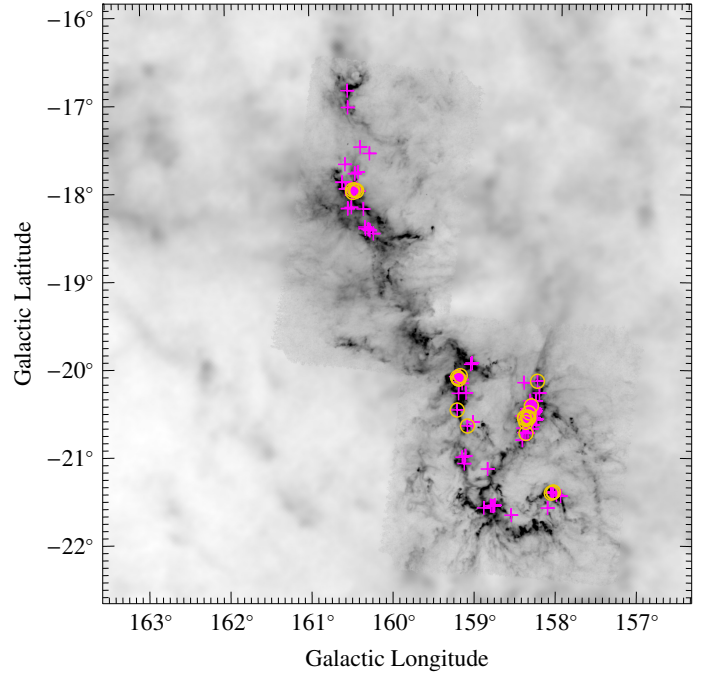

Fig. 14. Spatial distribution of the candidate Class I (pink crosses) and Class 0 objects (orange circles, see Sadavoy et al. 2014) used to estimate the Schmidt law.

Class I protostars. Furthermore, we can observe the similarity with Koenig criteria.

To find YSO candidates that are associated with known objects, we cross-checked our selection with the SIMBAD astronomical database and with the catalogs by Evans et al. (2009), Gutermuth et al. (2008, 2009), Jørgensen et al. (2006), Kirk & Myers (2011), Winston et al. (2009) and Young et al. (2015), based on *Spitzer* data. Many sources selected through WISE data analysis have already been included in other catalogs. Nevertheless, the complete sky coverage of the WISE satellite allows us to study regions that are parts of the cloud but that were never observed by *Spitzer*. The final selection consists of previously identified *Spitzer* sources that are merged with newly identified WISE objects. Using WISE data, 61 new sources were selected, of which 17 belong to IC 348 and just one to NGC 1333.

We now focus on the candidate Class I protostars, that were selected previously with our colour−colour diagrams. To further analyse these sources, in particular to test whether our classification scheme is reliable, it is useful to study their spatial distribution. Figure 13 shows the positions of the Class I protostars that were selected through the [3.4]−[4.6] vs. [4.6]−[12] and [3.4]−[4.6] vs. [4.6]−[22] diagrams. All sources (except one) are placed in the highest opacity regions: this agrees well with the hypothesis that they are located close to their original place of formation. Most of Class I YSOs selected through the [3.4]−[4.6] vs. [4.6]−[12] diagram are situated in the NGC 1333 region. This could imply, as Jørgensen et al. (2006) observed, that the age of NGC 1333 is slightly lower than the age of IC 348: indeed, it is estimated that IC 348 is 2 Myr old (Muench et al. 2007), while NGC 1333 does not exceed 1 Myr (Lada et al. 1996). We already noted that the number of sources selected with the [3.4]−[4.6] vs. [4.6]−[22] is lower than for the [3.4]−[4.6] vs. [4.6]−[12] diagram. Class I protostars in [3.4]−[4.6] vs. [4.6]−[12] diagram correspond to

Class I protostars in [3.4]−[4.6] vs. [4.6]−[22] diagram, except for three sources that are not detected in the first diagram. Surprisingly, the [3.4]−[4.6] vs. [4.6]−[22] diagram does not detect any Class I protostar in NGC 1333. We evaluated the cloud temperature and optical depth at each object position. We excluded from the WISE selection all the objects in areas with optical depth $\tau < 3.141 \times 10^{-5}$ (corresponding to $A_K < 0.1$ mag), supposing that this level of optical depth corresponds to the cloud boundaries. Figure 14 shows the final selection of Class I and Class 0 protostars (139 sources). Only two of the new sources selected by WISE are classified as Class I protostars. All the other sources in the figure have been previously classified using *Spitzer* data. We note that for some sources our classification differs to the one obtained by *Spitzer* catalogs. In these cases, we decided to follow the *Spitzer* classification.

5.2. Determining the Schmidt law

We computed the extinction at each source position using our *Herschel*-derived extinction map and binned them in log-spaced bins. Then we evaluated the cloud area between two consecutive extinction levels and the number of sources included within them. In this way, we evaluated the protostar surface density, Σ_{YSO}, as a function of the extinction, as the number of sources between two consecutive extinction levels divided by the corresponding area. Since the gas surface density Σ_{gas} is proportional to the K-band extinction (see Eq. (9)), it is possible to express the Schmidt law as

$$\Sigma_{YSO} = \kappa A_K^\beta, \tag{18}$$

where Σ_{YSO} is simply equal to $\Sigma_{SFR} \times \tau$, and τ is the mean age of a Class I/0 protostar. Figure 15 represents the Schmidt law for the Perseus molecular cloud. The values obtained for the parameters are

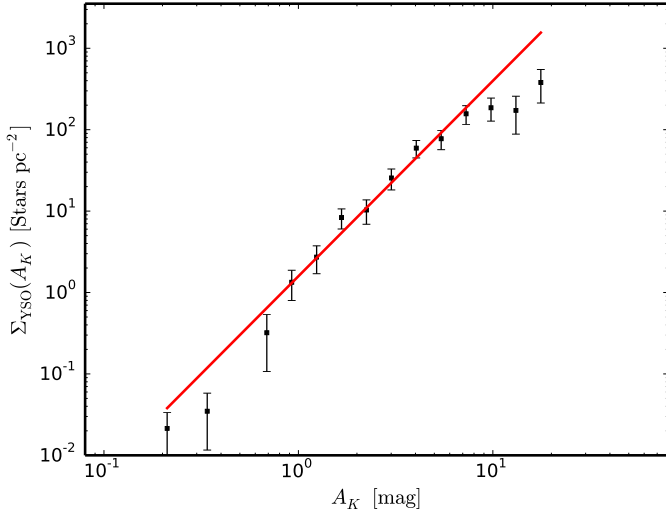$$\begin{cases} \kappa = 0.2 \pm 0.07 \, [\text{YSO pc}^{-2} \, \text{mag}^{-\beta}], \\ \beta = 2.4 \pm 0.6. \end{cases} \tag{19}$$

Fig. 15. Schmidt law in the Perseus molecular cloud. Here, $\Sigma_{\mathrm{YSO}} \propto A_K^{2.4}$, and $A_K \propto \Sigma_{\mathrm{gas}}$.
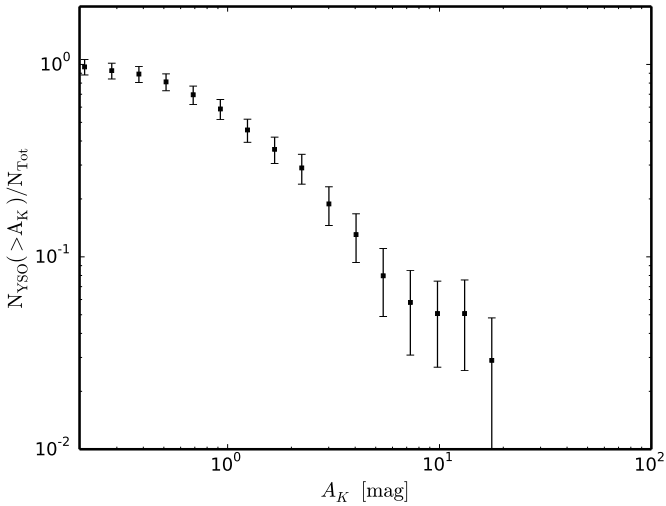

Fig. 16. Cumulative protostellar function in the Perseus cloud as a function of A_K, i.e. $N_{\mathrm{YSO}}(>A_K)$.

The value we found for β is steeper (although compatible) to what is reported by Lombardi et al. (2014) for the Orion molecular cloud complex and by Lada et al. (2013) for the Taurus molecular cloud. Indeed, Lombardi et al. (2014) find $\beta = 1.99 \pm 0.05$ for Orion A and $\beta = 2.16 \pm 0.10$ for Orion B, while Lada et al. (2013) find $\beta = 2.09 \pm 0.14$ for Taurus. Even though the Schmidt law is a useful tool to understand the star formation inside the cloud, it does not completely describe the whole process. For this purpose, we considered the function that represents the cumulative number of sources above a certain extinction A_K as a function of that extinction, as shown in Fig. 16. Even though the Schmidt law predicts that the surface density of protostars steeply grows with extinction, the effective number of protostars decreases as the extinction increases, similar to observations of the Orion molecular cloud in Lada et al. (2013).

The total number of protostars is defined as (Lada et al. 2013)

$$N_{\mathrm{YSO}} = \int \Sigma_{\mathrm{YSO}}(A_K)\mathrm{d}S = \int \Sigma_{\mathrm{YSO}}(A_K)|S'(>A_K)|\mathrm{d}A_K. \quad (20)$$

Indeed, the number of protostars at a given extinction level is the product of the area $S(A_K)$, which encompasses that extinction level, and $\Sigma_{\mathrm{YSO}}(A_K)$. The total number of protostars is given by the integral of this product over all extinction in the cloud. Changing the integration variable from S to A_K gives Eq. (20). We already studied the function $S(>A_K)$ (Fig. 7) and we concluded that its trend is $\propto A_K^{-2}$ and therefore $S'(>A_K) \propto A_K^{-3}$. Thus, the number of protostars formed within the cloud not only depends on the surface density of the gas but also on the area function and its derivative of the integral area function, i.e. the (unnormalized) PDF. As Lombardi et al. (2015) show, the PDFs of a sample of nearby molecular clouds, including Perseus, roughly follow the same profile, with slopes in logarithmic binning between ~-2 and ~-4, which correspond to slopes between ~-3 and ~-5 in the linear binning that was performed here. Therefore, it is conceivable to assume that, if the clouds have the same PDF and the same Schmidt law, then the function that describes the number of protostars above a certain extinction (normalized to the total number of protostars) is roughly the same for all the clouds.

6. Conclusions

Our main results are as follows:

- We produced optical depth and temperature maps of the Perseus molecular cloud, obtained using the data from the *Herschel* and *Planck* satellites. The maps have a 36 arcsec resolution for *Herschel* observations and a 5 arcmin resolution elsewhere.
- We calibrated the optical depth maps using 2MASS/ NICEST extinction data and we obtained extinction maps at the resolution of *Herschel* with a dynamic range of 1×10^{-2} mag to 20 mag of A_K. In particular, we evaluated the ratio $C_{2.2}/\kappa_{850} = 3620 \pm 252$, i.e. the ratio between the 2.2 μm extinction coefficient and of the 850 μm opacity.
- We studied the cumulative and differential area functions of the data, and we showed that, starting from $A_K \simeq 0.1$ mag, the cumulative area function follows a power law with index $\simeq -2$.
- We used WISE data to improve current YSO catalogs that are mostly based on *Spitzer* data and we built an up-to-date selection of Class I/0 protostars.
- We evaluated the local Schmidt law, $\Sigma_{\mathrm{YSO}} \propto A_K^{\beta}$, using the *Herschel*/*Planck* maps and the new object selection. We found that $\beta = 2.4 \pm 0.6$.
- We showed that the Schmidt law does not completely describe the whole star-formation process. Indeed, the total number of protostars effectively formed within a cloud depends on the surface area function $S(>A_K)$ and its derivative.

References

Andersson, B.-G., Wannier, P. G., Moriarty-Schieven, G. H., & Bakker, E. J. 2000, AJ, 119, 1325

André, P., Men'shchikov, A., Bontemps, S., et al. 2010, A&A, 518, L102

Astropy Collaboration, Robitaille, T. P., Tollerud, E. J., et al. 2013, A&A, 558, A33

Bachiller, R., & Cernicharo, J. 1984, A&A, 140, 414

Bally, J., Walawender, J., Johnstone, D., Kirk, H., & Goodman, A. 2008, The Perseus Cloud, ed. Bo. Reipurth, 308

Bigiel, F., Leroy, A., Walter, F., et al. 2008, AJ, 136, 2846

Cernis, K. 1990, Ap&SS, 166, 315

Cernis, K. 1993, Baltic Astron., 2, 214

de Zeeuw, P. T., Hoogerwerf, R., de Bruijne, J. H. J., Brown, A. G. A., & Blaauw, A. 1999, AJ, 117, 354

Enoch, M. L., Sargent, A. I., Golwala, S., Evans, II, N. J., & Young, K. 2006, in ASP Conf. Ser. 357, eds. L. Armus, & W. T. Reach, 137

Evans, N. J., Dunham, M. M., Jorgensen, J. K., et al. 2009, VizieR Online Data Catalog, J/ApJS/181/321

Evans, II, N. J., Heiderman, A., & Vutisalchavakul, N. 2014, ApJ, 782, 114

Griffin, M. J., Abergel, A., Abreu, A., et al. 2010, A&A, 518, L3

Griffin, M. J., North, C. E., Schulz, B., et al. 2013, MNRAS, 434, 992

Gutermuth, R. A., Myers, P. C., Megeath, S. T., et al. 2008, ApJ, 674, 336

Gutermuth, R. A., Megeath, S. T., Myers, P. C., et al. 2009, ApJS, 184, 18

Gutermuth, R. A., Pipher, J. L., Megeath, S. T., et al. 2011, ApJ, 739, 84

Harvey, P. M., Henning, T., Liu, Y., & Wolf, S. 2014, ApJ, 795, 21

Hatchell, J., Richer, J. S., Fuller, G. A., et al. 2005, A&A, 440, 151

Heiderman, A., Evans, II, N. J., Allen, L. E., Huard, T., & Heyer, M. 2010, ApJ, 723, 1019

Herbig, G. H., & Jones, B. F. 1983, AJ, 88, 1040

Hirota, T., Bushimata, T., Choi, Y. K., et al. 2008, PASJ, 60, 37

Jørgensen, J. K., Harvey, P. M., Evans, II, N. J., et al. 2006, ApJ, 645, 1246

Kennicutt, Jr., R. C. 1998, ApJ, 498, 541

Kirk, H., & Myers, P. C. 2011, ApJ, 727, 64

Kirk, H., Johnstone, D., & Di Francesco, J. 2006, ApJ, 646, 1009

Koenig, X. P., Leisawitz, D. T., Benford, D. J., et al. 2012, ApJ, 744, 130

Lada, C. J. 2015, IAU Symp., 309, 31

Lada, C. J., Alves, J., & Lada, E. A. 1996, AJ, 111, 1964

Lada, C. J., Lombardi, M., Roman-Zuniga, C., Forbrich, J., & Alves, J. F. 2013, ApJ, 778, 133

Lombardi, M. 2009, A&A, 493, 735

Lombardi, M., Lada, C. J., & Alves, J. 2010, A&A, 512, A67

Lombardi, M., Lada, C. J., & Alves, J. 2013, A&A, 559, A90

Lombardi, M., Bouy, H., Alves, J., & Lada, C. J. 2014, A&A, 566, A45

Lombardi, M., Alves, J., & Lada, C. J. 2015, A&A, 576, L1

Mainzer, A., Bauer, J., Grav, T., et al. 2011, ApJ, 731, 53

Muench, A. A., Lada, C. J., Luhman, K. L., Muzerolle, J., & Young, E. 2007, AJ, 134, 411

Ott, S. 2010, in Astronomical Data Analysis Software and Systems XIX, eds. Y. Mizumoto, K.-I. Morita, & M. Ohishi, ASP Conf. Ser., 434, 139

Pezzuto, S., Elia, D., Schisano, E., et al. 2012, A&A, 547, A54

Planck Collaboration XI. 2014, A&A, 571, A11

Poglitsch, A., Waelkens, C., Geis, N., et al. 2010, A&A, 518, L2

Rebull, L. M., Koenig, X. P., Padgett, D. L., et al. 2011, ApJS, 196, 4

Ridge, N. A., Schnee, S. L., Goodman, A. A., & Foster, J. B. 2006, ApJ, 643, 932

Sadavoy, S. I., Di Francesco, J., André, P., et al. 2012, A&A, 540, A10

Sadavoy, S. I., Di Francesco, J., André, P., et al. 2014, ApJ, 787, L18

Schlafly, E. F., Green, G., Finkbeiner, D. P., et al. 2014, ApJ, 786, 29

Schmidt, M. 1959, ApJ, 129, 243

Skrutskie, M. F., Cutri, R. M., Stiening, R., et al. 2006, AJ, 131, 1163

Taylor, M. B. 2005, in Astronomical Data Analysis Software and Systems XIV, eds. P. Shopbell, M. Britton, & R. Ebert, ASP Conf. Ser., 347, 29

Winston, E., Megeath, S. T., Wolk, S. J., et al. 2009, AJ, 137, 4777

Wright, E. L., Eisenhardt, P. R. M., Mainzer, A. K., et al. 2010, AJ, 140, 1868

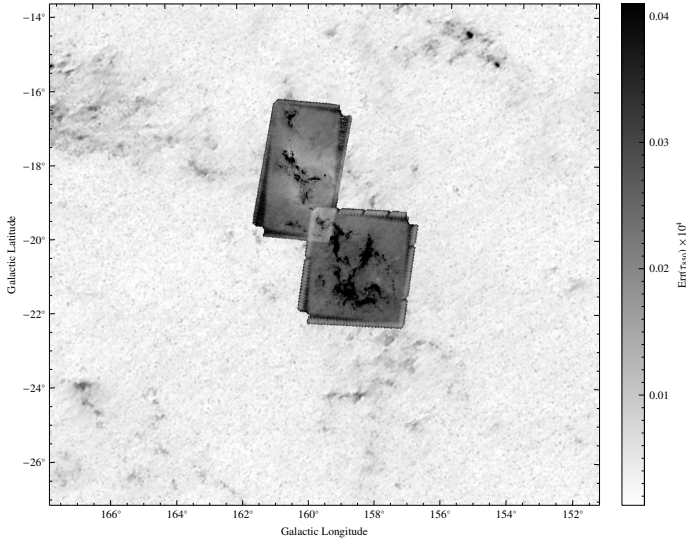Young, K. E., Young, C. H., Lai, S.-P., Dunham, M. M., & Evans, N. J. II 2015, AJ, 150, 40

Fig. A.1. Error on the optical depth map (see Fig. 3).
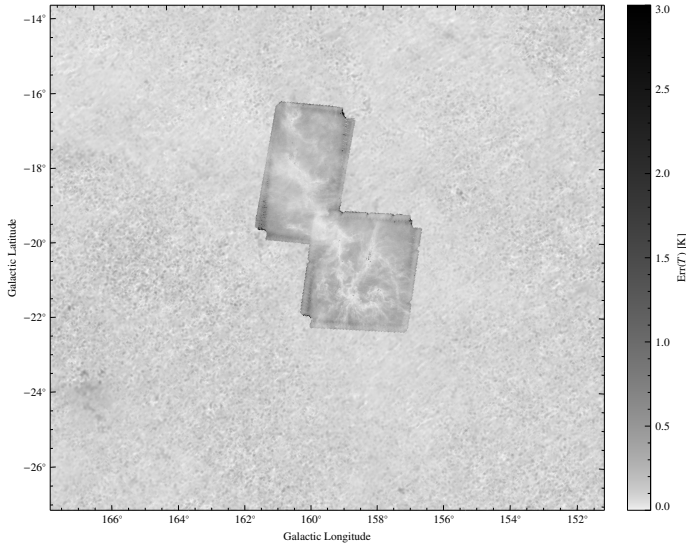
Fig. A.2. Error on the effective dust temperature map (see Fig. 4).

Appendix A: Hidden layers of multiple layer figures

In this section we provide a "flat" version of the hidden layers of multiple-layer figures.
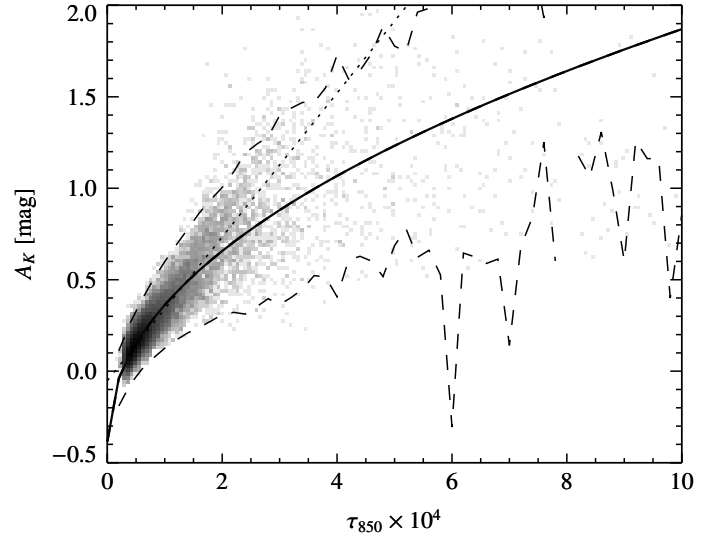
Fig. A.3. Relation between 353 GHz optical depth and the infrared NICEST extinction map, for $\tau_{850} \times 10^4 \leq 10$. The relation deviates from the linearity for high extinction values, as shown by the fit (solid line). The dashed lines represent the expected 3σ region. We also report in this plot the linear fit shown in Fig. 5 (dotted line).

Appendix B: Potential new star cluster

While analysing the spatial distribution of the WISE excess sources, we noticed a small group slightly offset from the cloud, whose centre is located at approximately $l = 162.2°$, $b = -19.4°$. We found no reference in the literature to this, potentially, new group of young stars. The group contains 14 members spread across an area of about one square degree. None of the excess sources is present in the HIPPARCOS catalog, it is therefore not possible to give an estimate of its distance or its potential relation with the Perseus molecular cloud. Follow up observations for this new group of excess sources is needed. The *Gaia* mission is expected to dramatically improve the distance determination for faint stars, which will allow for a better understanding of the origins and relevance of this group to the history of star formation in the Perseus region.

Appendix C: Catalog of the sources used to evaluate the Schmidt law

In this section we provide the list of protostars used to evaluate the Schmidt law. We report the position for all the sources and the WISE magnitudes for the sources detected by both *Spitzer* and WISE.

Table C.1. Catalog of the protostars used to determine the Schmidt law.

RA J2000 [deg]	Dec J2000 [deg]	$W1$ [mag]	$W2$ [mag]	$W3$ [mag]	$W4$ [mag]	Ref.
55.8726234	31.8720837	12.18 ± 0.03	10.55 ± 0.02	6.66 ± 0.02	7.5 ± 0.2	Y15
55.9000816	31.8358345					Y15
55.9382095	32.0662766					Y15
55.9625816	32.0522499					Y15
55.9868317	32.0513039					Y15
56.0109596	32.0331955					Y15
56.0383339	32.0438347	10.94 ± 0.04	9.66 ± 0.07	6.6 ± 0.1	7.1 ± 0.1	Y15
56.0540848	32.0265274					Y15
56.0889587	31.9923897					Y15
56.1035004	32.2301102					Y15
56.1262512	32.1931114					Y15
56.1805000	32.0254173	8.63 ± 0.03	6.93 ± 0.03	4.4 ± 0.07	8.5 ± 0.3	Y15
56.1831665	32.0267220					Y15
56.3075829	32.2027779					Y15
52.1356659	31.1847496	13.47 ± 0.04	11.88 ± 0.04	8.92 ± 0.07	8.0 ± NaN	Y15
52.1437073	31.0141945					Y15
52.1545410	31.2252235					Y15
52.1615829	31.3018322					Y15
52.1629181	31.1004734					Y15
52.1654587	31.2921944	11.43 ± 0.05	9.66 ± 0.04	6.96 ± 0.09	8.0 ± 0.3	Y15
52.1692924	31.2990265					Y15
52.1803322	31.2924709					Y15
52.2032089	31.2691116	13.50 ± 0.03	11.99 ± 0.03	9.2 ± 0.1	8.0 ± NaN	Y15
52.2135849	31.2942486					Y15
52.2314568	31.2435284					Y15
52.2358322	31.1269455					Y15
52.2383766	31.2386398					Y15
52.2434578	31.3715286					Y15
52.2467918	31.3423615					Y15
52.2471657	31.2635269					Y15
52.2522926	31.2002239					Y15
52.2565002	31.3390560					Y15
52.2638741	31.3873882					Y15
52.2657509	31.2677212	6.71 ± 0.06	4.93 ± 0.06	1.26 ± 0.01	−1.71 ± 0.002	Y15
52.2669182	31.2462502					Y15
52.2706261	31.3439999					Y15
52.2824173	31.3659172					Y15
52.2873764	31.3822498					Y15
52.2879181	31.3579731					Y15
52.2937088	31.2252789					Y15
52.2943764	31.2277775					Y15
52.2944984	31.3057213					Y15
52.2969170	31.3087215					Y15
52.2995415	31.3575001					Y15
52.3002510	31.2181664					Y15
52.3002510	31.2171402					Y15
52.3040428	31.3039722	10.38 ± 0.04	7.61 ± 0.09	5.65 ± 0.07	7.5 ± 0.15	Y15
52.3064156	31.2328339					Y15
52.3215408	31.4629173					Y15
52.3260841	31.3888607					Y15
52.3277931	31.3382511					Y15
52.3335838	31.4020824					Y15

Notes. Y15 stands for Young et al. (2015), G09 for Gutermuth et al. (2009), GMM09 for Gutermuth et al. (2008), E09 for Evans et al. (2009) and S14 for Sadavoy et al. (2014).

Table C.1. continued.

RA J2000 [deg]	Dec J2000 [deg]	*W*1 [mag]	*W*2 [mag]	*W*3 [mag]	*W*4 [mag]	Ref.
52.3351669	31.3094997					Y15
52.3503761	31.3326683					Y15
51.3313332	30.5733891					Y15
51.3429985	30.7538605					Y15
51.4009171	30.7543602					Y15
51.4020424	30.7561665					Y15
51.4117928	30.7350559					Y15
51.4129982	30.7328339					Y15
51.6561241	30.2578049					Y15
51.9128342	30.2175274					Y15
51.9301262	30.2080288					Y15
51.9486237	30.2012501	7.4 ± 0.2	6.07 ± 0.03	3.46 ± 0.01	1.64 ± 0.02	Y15
52.0016251	30.1336937					Y15
52.1437073	31.0141945					Y15
52.1887512	31.0949726	13.81 ± 0.02	11.63 ± 0.02	8.89 ± 0.08	8.7 ± NaN	Y15
52.2752075	30.5108891					Y15
52.3478317	31.5581932					Y15
52.4659157	31.6516666					Y15
52.5630836	30.3970547					Y15
52.5935402	31.5445824					Y15
52.6130829	30.4749451	10.8 ± 0.03	9.94 ± 0.02	7.39 ± 0.04	7.4 ± 0.1	Y15
52.6361656	30.4407215					Y15
52.8112488	30.8320560	9.93 ± 0.03	8.82 ± 0.03	6.39 ± 0.07	6.0 ± 0.1	Y15
52.8374176	30.7583618					Y15
53.0748329	30.8298626					Y15
53.1215401	31.0446663					Y15
53.2410011	31.1023064					Y15
53.2767067	31.1346111					Y15
53.2898331	31.0920010					Y15
53.3035011	31.3567219	7.28 ± 0.04	5.73 ± 0.04	3.11 ± 0.01	0.93 ± 0.02	Y15
53.3074989	31.3348064					Y15
53.3099174	31.1196938					Y15
53.3185005	31.1145840					Y15
53.3193741	31.1320000					Y15
53.3243752	31.1588612					Y15
53.3346672	31.1226387	13.55 ± 0.02	10.19 ± 0.02	8.2 ± 0.1	8.7 ± NaN	Y15
53.3637085	31.1194992					Y15
55.4212074	31.8012772					Y15
55.4821243	31.8031654					Y15
55.4944572	31.8059444					Y15
55.5090408	31.8005829					Y15
55.7335434	31.9457760					Y15
56.1472511	32.4770012					Y15
56.7726250	32.7190285	9.6 ± 0.02	8.22 ± 0.02	5.72 ± 0.04	8.9 ± 0.5	Y15
56.9232483	32.8622475					Y15
52.1438332	31.1181946					G09
52.3001671	31.2172222					G09
52.3428345	31.2318058					G09
52.2390404	31.237833					G09
52.203167	31.2691383	13.50 ± 0.03	11.99 ± 0.03	9.25 ± 0.13	8.6 ± NaN	G09
52.1802902	31.2925282					G09
52.2034988	31.2982502					G09
52.237957	31.319973					G09
52.3048325	31.3303623					G09
52.2471237	31.3356113					G09
52.2705841	31.3440571					G09
52.2378769	31.3569717					G09

Table C.1. continued.

RA J2000 [deg]	Dec J2000 [deg]	*W*1 [mag]	*W*2 [mag]	*W*3 [mag]	*W*4 [mag]	Ref.
52.2872925	31.3823051					G09
52.3814163	31.4243889					G09
55.9001236	31.8358345					G09
56.0540848	32.0265274					G09
56.0098763	32.027916					G09
55.9965401	32.0474701					G09
55.9382095	32.0662766					G09
55.9778328	32.075695					G09
56.1262512	32.1931381					G09
56.2982101	32.4647789					G09
52.2416000	31.3478000					GMM09
52.2879000	31.3849000					GMM09
55.9791985	32.0175018					E09
55.9886017	32.0131989					E09
55.9855003	32.0147018					E09
55.9902	32.0124016					E09
55.9908981	32.0533981					E09
55.9975014	32.0098991					E09
55.9985008	32.0317001	7.5 ± 0.1	6.21 ± 0.03	4.10 ± 0.03	6.12 ± 0.05	E09
56.0890007	31.9923992					E09
55.5444984	31.7849007	13.09 ± 0.03	11.93 ± 0.05	10.48 ± 0.04	8.0 ± NaN	E09
53.196701	30.9878998	8.79 ± 0.02	7.64 ± 0.02	5.78 ± 0.08	8.0 ± NaN	E09
51.9094429	30.2329445	9.58 ± 0.02	8.27 ± 0.02	6.51 ± 0.03	8.7 ± 0.5	E09
51.3975	30.7589					S14
52.2575	31.2594					S14
52.3283	31.3867					S14
53.3387	31.1242					S14
51.2893562	30.7727299	8.43 ± 0.02	6.92 ± 0.02	4.2 ± 0.1	8.6 ± 0.5	New
55.5620079	31.7993259	13.94 ± 0.02	12.33 ± 0.03	9.92 ± 0.04	7.3 ± 0.2	New